Measurement of Refractive Index at Cryogenic Temperature of Absorptive Silver Thin Films Used as Reflectors in a Fabry-Perot Cavity

KEVIN ROSENZIVEIG,[1,*] VALÉRIE SOUMANN,[1] PHILIPPE ABBÉ,[1] BENOÎT DUBOIS,[3] PIERRE-FRANÇOIS COHADON,[2] NICOLAS PASSILLY[1] AND SERGE GALLIOU[1]

[1] *FEMTO-ST Institude, Univ. Bourgogne Franche-Comté, CNRS, ENSMM, Besançon, 25030, France*
[2] *Laboratoire Kastler Brossel, Sorbonne Université, CNRS, ENS - Université PSL, Collège de France, Paris, 75005, France*
[3] *FEMTO Engineering, 15B avenue des Montboucons, 25030 Besançon Cedex, France*
[*] *kevin.rosenziveig@femto-st.fr*

Abstract: Data about the refractive index of silver thin films is scarce in the literature, and largely dependent on both the deposition method and thickness. We measure the refractive index of silver films at cryogenic temperature with a technique that takes advantage of the absorption of the films and the corresponding peculiar properties of Fabry-Perot cavities: a frequency shift between the reflection and transmission peaks, together with a modified cavity bandwidth. We demonstrate a $40-60\%$ decrease of the real value of the refractive index, together with a $5-9\%$ decrease for its imaginary value at 4 K.

1. Introduction

Knowledge of the refractive index and of the optical properties of any specific material in a particular geometry and condition is a problem that sparks interest among diverse communities including broad-spectrum opticians [1] [2] [3] as well as the plasmonics community [4] [5] [6].

Quartz Resonators (QR) can display very high mechanical quality factors Q at cryogenic temperature [7] and are therefore promising for ultrastable time reference [8]. To this end, a very high Q is not sufficient, a temperature-compensated quartz crystal cut (as defined in [9]) is required: such a cut is found at 4 K [10]. QR are commonly metal-coated with thin film electrodes for actuation and electrical sensing, with chromium and gold as the most common choice, but such electrodes can actually be used as optical mirrors as well, as metals usually have a high reflectivity at telecom wavelength (1550 nm). Compared to dielectric coatings, however, these thin metallic films still suffer from absorption. We study in the following how the peculiar properties of such optical cavities allow to measure the refractive index of the thin films at the telecom wavelength. Silver constitutes the most reflective metal at this wavelength and is therefore selected for the following study.

Optomechanical coupling can be taken advantage of to actuate the QR instead of piezoelectricity, but a solid knowledge on the refractive index of the thin films is then required.Indeed, the optical power is critical to achieve optomechanical coupling between mechanical modes and optical fields, be it in the frameworks of cavity optomechanics with radiation pressure or electrostriction [11] [12] [13] [14] [15]. The amount of light reflected and absorbed by a metal is dependent on its temperature [16] [17] [18] [19] with a trend for reflectivity to increase and for absorption to decrease at low temperature, which is appropriate with our goal to eventually use the QR at cryogenic temperature. These features are investigated through the peculiar properties of Fabry-Perot cavities with absorptive mirrors [20] [21] [22].

The standard method to measure the optical dielectric function (hence the refractive index) of

many thin-film materials, dielectric or metals is ellipsometric measurement [23] [24] [25] [26]. This requires to be able to measure a light beam incident on the sample through several angles, which may turn out to be complicated experimentally in a cryogenic environment.

In this work, some silver thin films deposited on the QR are investigated and we compare the refractive index at 1550 nm (telecom wavelength) at both room temperature and cryogenic temperature, i.e. at about 4 K, through an original method which relies on the specifics of absorbing mirrors used as a *Fabry-Perot* cavity. The method is limited to low-thickness absorptive layers, in conditions where a resonance signal can be observed from the Fabry-Perot cavity. This fits our experimental requirement of a fixed sample standing in the vacuum chamber, with the cryo-cooler turned on or off, to probe the room temperature or cryogenic temperature properties of the thin film. Moreover, measuring the mean refractive index, i.e. averaged over the two deposited layers as well as over the whole surface that the light acts upon is a drawback for absolute knowledge over material property; it does, however, fulfill our purpose to have a clear idea of the equivalent layer for the *Fabry-Perot* cavity.

Through the measurement of the frequency shift between the transmitted and reflected peaks [20] [15] and the Full Width at Half Maximum (FWHM) of the transmitted peak (see Fig. 1), it is possible to retrieve the complex refractive index $\tilde{n} = n - ik$. We first give details about the principle of the technique and some estimates of the order of magnitude, then describe the experimental setup and numerical methods in the next section. The following section displays the derived refractive indices, followed by an analysis of the different sources of uncertainty.

2. Experiment and Methods

The refractive index is expressed as a 2D quantity, $\tilde{n} = n - ik$. The real and imaginary part of the refractive index can be considered as two independent quantities to retrieve, implying the need of the two following variables to retrieve them from: the full width at half maximum (FWHM) and the frequency shift of the resonance Δf. We first remind some results about absorptive Fabry-Perot cavities, then proceed with details about the method to retrieve $\tilde{n}$ before presenting the setup used for the measurements.

2.1. Absorptive Fabry-Perot cavity

The Fabry-Perot system is represented within the whole experimental setup in Fig. 2(a) while the quartz resonator is depicted on Fig. 2(b) and the resonator within its holder is shown on Fig. 2(c). It has been described theoretically [20] [21], from which we use the notation to express most of the following quantities.

The thin layers of silver are considered to be similar both in thickness and in refractive index. The refractive index of any layer (quartz is layer 2, silver layer 1 and air layer 0) is noted $\tilde{n}_j = n_j - ik_j$.

The transmitted intensity is written:

$$\mathcal{T}_{FP} = \mathcal{T}_{\max} \frac{1}{1 + F \sin^2(\delta/2)} \tag{1a}$$

where we used

$$\mathcal{T}_{\max} = \frac{|T_{012}|^4}{(1 - |R_{210}|^2)^2} \tag{1b}$$

$$F = \frac{4|R_{210}|^2}{(1 - |R_{210}|^2)^2} \tag{1c}$$

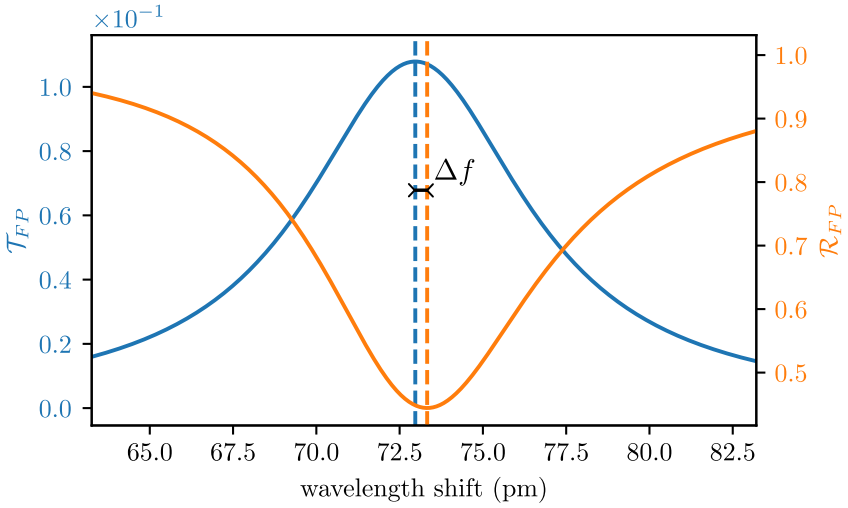

Fig. 1. *Calculated reflection and transmission curves of an absorptive Fabry-Perot cavity for two* 35 nm *thick layers of silver deposited on quartz, with a refractive index* $\tilde{n} = 0.2997283 - i10.7355059$ *taken fromhttps://www.overleaf.com/project/617aa0824dabff9f3a123407 [23]. The resonance is centered close to* 1550 nm. *The shift in frequency is noticeable here,* $\Delta\lambda = 0{,}35$ pm *which corresponds approximately to* $\Delta f = 45$ MHz.

and the reflected intensity can be expressed as:

$$\mathcal{R}_{FP} = |R_{012}|^2 \frac{1 + |\zeta_{210} R_{210}|^2 - 2|\zeta_{210} R_{210}| \cos\Delta}{1 + |R_{210}|^4 - 2|R_{210}|^2 \cos\delta} \tag{1d}$$

with the quantity ζ_{210}, which is emerging because of the non-typical *Stokes relations*, linking the reflection and transmission coefficients. This quantity is expressed as:

$$\zeta_{210} = \frac{R_{012}R_{210} - T_{012}T_{210}}{R_{012}} = |\zeta_{210}| e^{i\phi_{210}}$$

In Eqs. (1a) and (1d), the phase quantities Δ and δ appear, and are expressed as:

$$\Delta = 2\beta_2 - \phi_{210} - \Delta_{210} \tag{2a}$$
$$\delta = 2\beta_2 - 2\Delta_{210} \tag{2b}$$

The quantity T_{ijk} (R_{ijk}) has been repeatedly used in Eq. (1) and represents the transmission (reflexion) in a medium j sandwiched between two semi-infinite planes of media i and k, and is written:

$$T_{ijk} = \frac{t_{ij}t_{jk}e^{-i\beta_j}}{1 + r_{ij}r_{jk}e^{-2i\beta_j}} \tag{3a}$$

$$R_{ijk} = \frac{r_{ij} + r_{jk}e^{-i2\beta_j}}{1 + r_{ij}r_{jk}e^{-2i\beta_j}} = \left|R_{ijk}\right| e^{i\Delta_{ijk}} \tag{3b}$$

where the familiar quantities t_{ij}, r_{ij} and β_i are:

$$t_{ij} = \frac{2\tilde{n}_i}{\tilde{n}_i + \tilde{n}_j} \tag{3c}$$

$$r_{ij} = \frac{\tilde{n}_i - \tilde{n}_j}{\tilde{n}_i + \tilde{n}_j} \tag{3d}$$

$$\beta_i = \frac{2\pi}{\lambda_0}\tilde{n}_i d_i \tag{3e}$$

with λ_0 the vacuum wavelength, d_i the i^{th} layer's thickness. β_i represents the phase acquired over a distance d_i in a medium of refractive index $\tilde{n}_i$.

From Eqs. (1a), (1d) and (3), the optical refractive index $\tilde{n}_1$ of the silver thin layers influences the peaks themselves, by modifying both their FWHM and their exact location, in particular with respect to one another (hence their frequency shift Δf).

2.2. Method

In Eq. (1a), although $\beta_2 = \frac{2\pi}{\lambda_0}\tilde{n}_2 d = \frac{2\pi f}{c}\tilde{n}_2 d$ has a simple linear dependency on the frequency, Δ_{210} depends on the refractive indices of the metallic layers in its expression (see Eq. (3b)), although it barely varies with λ, so that it almost constitutes a constant in the equation over a wide range of wavelength. For example, varying λ between 1545 nm and1555 nm only gives a relative variation of $\mathrm{d}\Delta_{210} \approx 2{,}1 \times 10^{-4}$. Because we consider small wavelength or frequency variations from resonance in order to find the FWHM and Δf, the relative variations for Δ_{210} with the wavelength or frequency will be considered negligible in the following.

In this case, replacing β_2 in Eq. (2b) with its expression from Eq. (3e), the quantity δ is simply linearly dependent on the laser frequency:

$$\delta = \frac{4\pi f \tilde{n}_2 d}{c} + \delta_0(\tilde{n}_{\mathrm{Ag}}) \tag{4}$$

where δ_0 only depends on the wavelength through the mirrors' refractive index.

FWHM

According to the transmitted intensity equation Eq. (1a), as well as the previous observation about the quantity δ in Eq. (4), the FWHM for the absorptive case is derived by noting that the shift in frequency from resonance to half the peak's maximum is written:

$$F \sin\left(\frac{\mathrm{d}\delta^2}{2}\right) = 1$$

$$\frac{\mathrm{d}\delta}{2} \approx \sqrt{\frac{1}{F}}$$

where the phase shift $\mathrm{d}\delta$ corresponds to a laser frequency shift from the $\delta = 0$ condition of the resonance frequency. Using Eq. (4):

$$\mathrm{FWHM} \approx \frac{c}{\pi\tilde{n}_2 d}\sqrt{\frac{1}{F(\tilde{n}_{\mathrm{Ag}})}} \tag{5}$$

where the approximation sign holds in the high-reflectivity limit, which is always verified here experimentally. Let us stress the dependence of F on the refractive index of the metallic layer. Furthermore, although F depends on the wavelength, computing it against the wavelength shows, as for δ, that it only marginally depends on it, for the same reason as that concerning Δ_{210} before.

Note that although in the regular non-absorptive Fabry-Perot cavity the transmission and reflection peaks have the same FWHM, in the present case, the reflection peak is dissymetrical and the FWHM must therefore be considered for the transmission.

Δf

The expression for the reflected intensity is written in Eq. (1d). Contrary to the FWHM, knowledge about the resonance (i.e. transmission maximum) frequency is necessary to compare it to the reflection minimum frequency and define Δf from the difference. The difference between Δ and δ yields:

$$\Delta - \delta = \Delta_{210} - \Phi_{210} \tag{6}$$

This quantity as well is almost wavelength-independent.

With $\epsilon = \Delta - \delta$ being nearly constant with respect to wavelength, the optimum of Eq. (1d) can be found by rewriting it in the following form:

$$\mathfrak{R}_{\mathrm{FP}} = |R_{012}|^2 \frac{1 + |\zeta_{210} R_{210}|^2 - 2|\zeta_{210} R_{210}| \cos(\delta + \epsilon)}{1 + |R_{210}|^4 - 2|R_{210}|^2 \cos\delta}. \tag{7}$$

By considering δ as the variable and all the other quantities as constants, an optimum for the function exists. This optimum is defined as δ_R, and describes the phase for which the reflection is minimum (see the full expression in Appendix A). Δf is therefore the frequency shift between $\delta = 0$ and $\delta = \delta_R$.

Eq. (4) establishes that δ linearly depends on the frequency. The shift in δ is therefore written:

$$\mathrm{d}\delta = 4\pi\tilde{n}_2 d \frac{\mathrm{d}f}{c} \tag{8}$$

so that Δf corresponds to $\mathrm{d}\delta = \delta_R$, which allows to find the frequency shift:

$$\Delta f = \frac{c\ \delta_R(\tilde{n}_{\mathrm{Ag}})}{4\pi\tilde{n}_2 d} \tag{9}$$

where we stressed the dependence of δ_R on the refractive index of the mirror $\tilde{n}_{\mathrm{Ag}}$.

2.3. Computational method

Consequentely, Δf (Eq. 9) and the FWHM (Eq. 5) are two experimentally accessible variables from which to retrieve the actual refractive index. For each value of FWHM (Δf), there exists a priori an infinite set of solutions values n and k that verifies the condition.

We design a python program that computes the FWHM and the Δf over a certain n and k span for a particular mirror thickness (considered to be equal on both sides). Because the computational 2D surface of both FWHM and Δf is not a perfect plane over a large n and k span, it is not possible to resolve it analytically by fitting it to a plane, and trying to do so leads to erroneous results. Instead, it is more accurate to consider a local numerical approximation solution, i.e. a couple of n_0 and k_0 can be considered a solution for the FWHM if they verify:

$$|\mathrm{FWHM}(n, k) - \mathrm{FWHM}(n_0, k_0)| < \eta \tag{10}$$

where η is an arbitrary precision to be specified for calculation. A visual representation of such a situation is presented in Fig. 3. Note that these calculations are lead with numpy 128bits floats; regular 64bits floats is responsible for dramatic numerical rounding errors and making Δf unusable. Indeed, Δf relies on several calculated quantities, which, when rounded, quickly lead to errors especially when calculating the phase of the reflection minimum at large thickness (see Eq. 13, with an arccos being particularly sensitive to rounding errors).

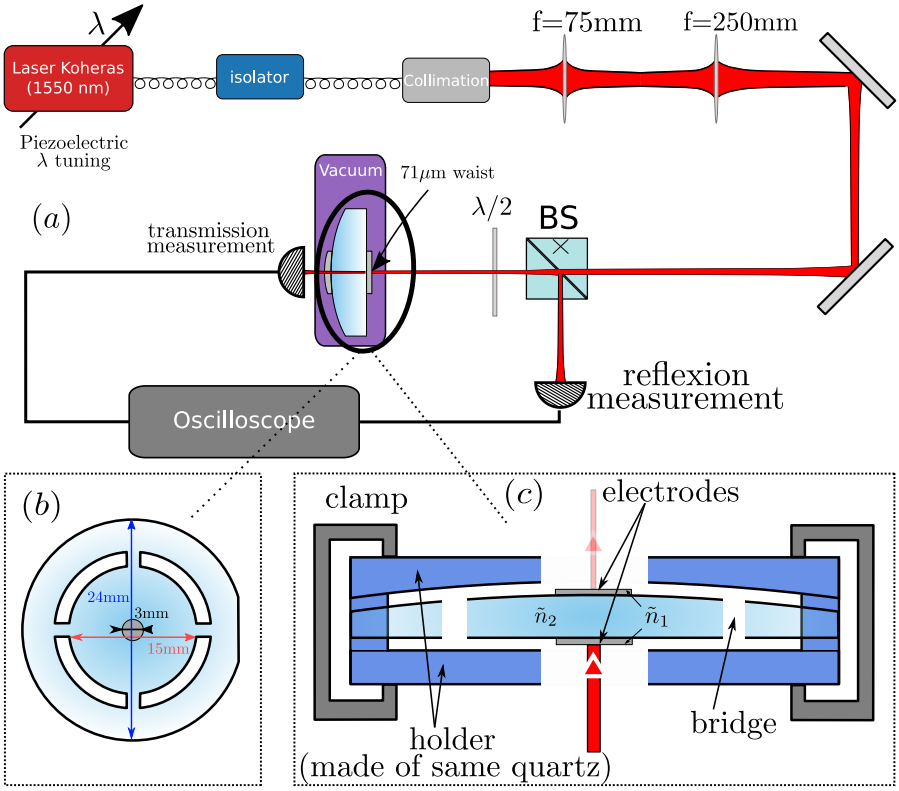

Fig. 2. *(a) Top view: experimental setup to measure the optical signal from the Fabry-Perot cavity. The tunable laser is collimated onto the optical table and is mode-matched to arrive onto the quartz where it gets partially reflected and partially transmitted through the Fabry-Perot cavity. The reflection and transmission signal are then measured and superimposed on an oscilloscope along with the voltage ramp used to modulate the laser's frequency. (b) Bottom-left view: front face of our quartz, with typical bridge-like structure to minimize losses near the center, the vibrating part. (c) Bottom-right view: BVA-like structure (*Boîtier à Vieillissement Amélioré*) for holding the quartz, with holes in the holder to allow for the laser beam to pass through. The metallic layer which typically serves as electrodes is used as mirrors here, with intrinsic absorption allowing for effects described throughout the main text and permitting n and k extraction. The refractive indices of the quartz ($\tilde{n}_2$) and silver thin layer ($\tilde{n}_1$) are noted here.*

Each of these two a priori semi-infinite sets of n_0 and k_0 that are solutions, with one for FWHM and the other for Δf, form a straight line locally (i.e. over a small enough span) . We fit them to a first order polynomial and calculate their intersection point. This point is the solution of the problem and gives $\tilde{n}_1 = \tilde{n}_{\mathrm{Ag}}$.

2.4. Experimental measurement

The FWHM and the peaks' frequency shift Δf are measured with the experimental setup presented in Fig. 2(a).

The laser is a commercially available *Koheras AdjustiK*, Continuous Wave centered at 1550 nm. It is power tunable, with a power output up to 120 mW, although an incident power of only

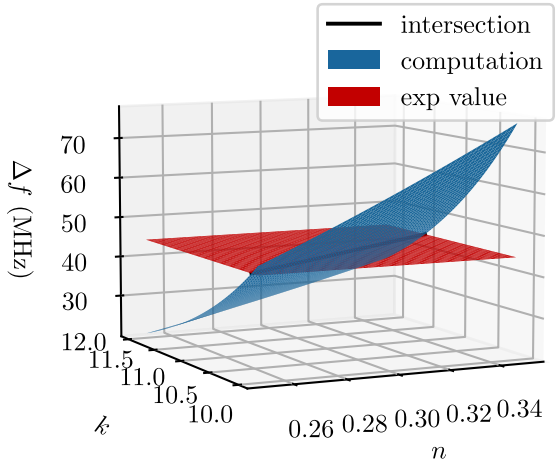

Fig. 3. *A typical extraction of sets of n and k that verifies the experimental value conditions, for* Δf*. Similar behaviour is obtained for the FWHM. This produces a locally linear set of solutions, which are a priori different than the ones for FWHM, except for their intersection, which therefore leads to the actual value of* $\tilde{n}_{Ag}$*. In this example, the theoretical values of FWHM and* Δf *for a* 35 nm*-thick layer of silver are calculated from [23],* $\tilde{n} = 0.2997 - 10.7355j$*. This value of* $\tilde{n}$ *corresponds to FWHM=*1011 MHz *and* $\Delta f = 45$ MHz*,* $\eta = 1 \times 10^{-2}$ *(Eq. 10). The program returns a fit value of* $\tilde{n} = 0.2999 - 10.7384$*, i.e. an error of approximately* 7×10^{-4} *for n and* 3×10^{-4} *for k. Note that the calculation is lead with 128bits numpy floats (see main text).*

5 mW is used for the following measurements. It is also wavelength-tunable (about 1 nm range) through a piezoelectric input voltage port. A high-voltage ramp (linearly varying) input signal establishes a frequency sweeping velocity, permitting to transform the time-varying signal into a frequency-varying signal.

The photodiode *Thorlabs* PDA20CS(-EC) for transmitted signal measurements is set with 0 dB gain for the 35 nm and 50 nm thickness silver layers and 20 dB gain for the 75 nm layer (see section 3). The photodiode for the reflection, on the other hand, is a *Newport* 1611 photodiode, from which the DC output is retrieved. The photodiodes show a null phase difference when the laser power is modulated in the absence of a Fabry-Perot cavity, so that the phase difference we measure between the transmission and reflection peaks corresponds to an actual frequency shift between the peaks and not an artifact.

The depositions of silver thin films are made through Magnetron Sputtering Technology (MST) with machine MP500 from *Plassys*. Silver targets are 101,6 mm (4") in diameter. The deposition chamber is kept at 0,9 Pa with Argon. The DC sputtering power is 160 W with a deposition velocity of 130 nm/min.

At the laser's output in Fig. 2(a), the beam is mode-matched with a set of lenses to reach the required 71 µm beam size (waist) when it reaches the plane entrance mirror. The system is aligned by tilting the entrance injection mirror and the customed *Thorlabs Polaris* mirror holder, with the QR set inside (see Fig. 2 (b) and (c)). This only allows for an angular tuning range of about 2° for the input mirror.

The laser beam is then incident onto the QR, which is a plano-convex quartz crystal with

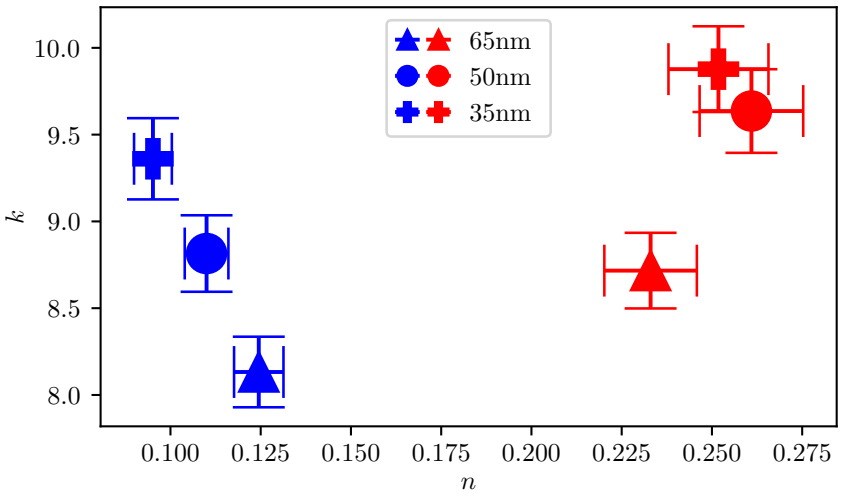

Fig. 4. *Graphical representation of the results displayed in Table 1. The red color (all the right-most points of the graph) is used for the* 300 K *points, whereas the blue color (all the left-most points of the graph) is used for the* 4 K *points. The error bars including the thickness uncertainty (see Table 4 and the* ***red bold error bars*** *displayed in the results Table 1) are taken here.*

250 mm curvature radius and 1 mm thickness at the centre. This amounts to a Free Spectral Range (FSR) of approximately 97 GHz. Since the QR is birefringent, the Beam Splitter (BS) used to retrieve the reflected signal is non-polarized whereas a $\lambda/2$ waveplate is added to control the incident polarization, so as to select the fast or slow axis of the QR and obtain coupling with only one of the polarization modes. We stress that the choice of using quartz here is dictated by the needs for later optomechanical coupling in order to achieve an ultrastable reference resonator, and that one could chose e.g. a glass substrate instead.

Based on the transmitted and reflected experimental signals, the oscilloscope allows to record the data and the FWHM and Δf are extracted through a python program that fits these curves with the theoretical model.

3. Results, Discussion

We present here some results for n and k for some specific deposition runs, both at room and cryogenic (4 K) temperature, extracted from experimental values for Δf and FWHM that are obtained with the setup shown in Fig. 2(a). It is not possible to measure the refractive index at intermediate temperatures because the cryocooler can only be set to 4 K. When the cryocooler is turned off, the temperature quickly changes so that there is no time to fine-tune the alignment and acquire the transmission and reflection measurement.

The measured values are processed, knowing the deposition thickness to obtain their corresponding n and k, and are tabulated with their respective uncertainty (see following section for details). Let us stress that each extracted value of n, k, FWHM and Δf correspond to a single particular deposition. The values are detailed in Table 1 and presented in Fig. 4. The measurements and method meet the ground requirement of clearly separating between the room temperature and the cryogenic temperature results, as the wide spread (including uncertainty bars) between the two results shows.

		300K	4K	FWHM (MHz) **at 300K**/*at 4K*	Δf (MHz) **at 300K**/*at 4K*
Ag35nm	n	0.2518 **±7.09%** *±5.79%*	0.0951 **±7.09%** *±5.79%*	**1226** *1005*	**50** *20*
	k	9.8772 **±3.39%** *±1.19%*	9.3608 **±3.39%** *±1.19%*		
Ag50nm	n	0.2609 **±6.09%** *±5.29%*	0.1100 **±6.09%** *±5.29%*	**790** *612*	**35** *13*
	k	9.6359 **±2.69%** *±1.49%*	8.8149 **±2.69%** *±1.49%*		
Ag65nm	n	0.2330 **±5.49%** *±4.89%*	0.1244 **±5.49%** *±4.89%*	**690** *500*	**31** *12*
	k	8.7164 **±2.49%** *±1.89%*	8.1323 **±2.49%** *±1.89%*		

Table 1. *Table of computations of n and k with their uncertainty, each for one particular deposition run. In green (first in order of appearance), the uncertainty taking into account the deposition thickness uncertainty; in orange (second in order of appearance), the uncertainty without taking into account the uncertainty on the deposition thickness (see discussion in section 3.2). These values are extracted from experimental values of FWHM and Δf (last columns), with the first value appearing in red being the* 300 K *value, whereas the value in blue is the* 4 K *value.*

For each thickness, there is a trend for both the real and imaginary parts of the refractive index to decrease at 4 K with respect to 300 K. The decrease is much more significant for the real part n ($\approx 40-60\%$) than for the imaginary part k ($\approx 5-8\%$). This is consistent with the trend found in the literature (with the data from e.g. [26]). Note that for a given temperature, the index also varies with the thickness, as widely observed in the literature [4] [18] [23]. Indeed, the refractive index change as a function of the silver thin film thickness is caused by the change in density of the film, which in turn may depend on the deposition process.

Our obtained values for 35 nm of silver, for example, vary by about 16% for n and 8% for k with respect to the values obtained in [23] at 1550 nm wavelength. This is consistent with what is found in the literature: the refractive index highly depends on the deposition process

and can vary, depending on this parameter, by as much as 60% for n and 8% for k at 500 nm wavelength (data from [26]). Comparing values for some $d \approx 35$ nm thin film at 594 nm from [4] and [23] permits to see that even though the technique of deposition is evaporation in both cases, the variation is still large: $\approx 45\%$ for n and $\approx 6\%$ for k. In view of these orders of magnitude, and although the wavelength in this work is different, we deem that the difference between the obtained values and the values found in [23] are in satisfying agreement.

The extraction method we use inherits an intrinsic imprecision from the fact that we consider the two mirrors as perfectly equal. In addition, we consider the mean refractive index over the illuminated area corresponding to the same beam waist 71 µm beam-waist on the plane mirror and on the concave mirror.

We chose to use a 1550 nm wavelength laser to investigate the refractive index for conveniency and accessible experimental supplies. Nevertheless, the extraction method used in this work can easily be extended to longer or shorter monochromatic wavelength. Because the technique uses the optical resonance, the requirement is to be able to sweep the frequency of the source over the resonance gain. This means that the laser source should be tunable in wavelength and that its spectral width should be narrower than the *Fabry-Perot* resonance's spectral width, in our case in the order of 500 MHz to 1200 MHz. Furthermore, there should be no intra-silver-layer resonance. The theoretical limit for this to happen is when $d = p \times \lambda/2$, with p any natural number, i.e. deep UV light in this case, so that the technique is usable down to this range of wavelength.

As previously mentioned, the evolution of the optical properties at 4 K go in the desired direction, i.e. become less absorptive and more reflective, in accordance with literature. For example, the Fabry-Perot cavity with 35 nm of silver on quartz has a (theoretical) optical finesse of 80 at room temperature, which grows up to 100 at 4 K. The maximum transmission is almost doubled, from 1% at room temperature to 1.8% at 4 K. The contrast of the reflection (i.e. $1 - R_{\min}/R_{\max}$) goes from 18% at room temperature to 65% at 4 K. The maximum absorption goes from 50% at room temperature to 40% at 4 K. All these quantities are therefore improved at 4 K, although this improvement seems insufficient to actuate an optomechanical coupling with radiation pressure in our case [15].

3.1. Errors and Uncertainties

We now discuss several types and sources for error and uncertainty in our results. Once all these sources of error and uncertainty are established, a *Monte-Carlo* type statistical analysis is performed to be able to account for the error bars displayed in the previous result section.

Intrinsic and Numerical

To verify the robustness of the method of extraction, a safety check for the validity of its output n and k is performed. Because n and k are extracted through the knownledge of FWHM and Δf, we start from a known n and k. The expected FWHM and Δf are then calculated through two different methods: one is the method presented in this paper, the other is a simple iterative method to find the optimum of the transmission and reflection peaks recursively. They are in good agreement, so that the possible error from FWHM and Δf calculation is not further taken into account as a source of uncertainty. These serve as an input of our method.

Table 2 shows the values obtained during this process, where the input n and k data are taken from [23]. Columns 1 and 2 display the known values for n and k. The calculated FWHM and Δf, in columns 3 and 4, are used to feed the program. This permits to obtain columns 5 and 6 with the n_{fit} and k_{fit}. Finally, columns 7 and 8 correspond to the relative error made between the program output and the original value. Note that these errors and all extracted set of n_0 and k_0 (solutions of the problem) depend slightly on the span of n and k when running the fit process. This is explained by the quality of the local linear fit, once intersection points are found between the computed surface of FWHM and Δf and the actual experimental value (see Fig. 3). For

example, for a 50 nm silver layer, with refractive index $N = 0.2522 - 10.8507j$, allowing n to be spanned between $0.24 < n < 0.26$ and $10.84 < k < 10.86$ gives the corresponding estimated error in Table 2, namely $1{,}4 \times 10^{-3}$ for n and 7×10^{-4} for k. Allowing for $0.07 < n < 0.32$ and $10 < k < 12$, however, increases this error to $3{,}9 \times 10^{-3}$ for n and 8×10^{-4} for k.

The results displayed in Table 2 show that the numerical extraction procedure provides satisfactory precision. In particular, the errors made from this source are much smaller than some other errors shown in this section. They are therefore discarded in the following.

	n	k	FWHM	Δf	n_{fit}	k_{fit}	$\delta n/n$	$\delta k/k$
Ag20nm	0.3130	10.6052	2841	128	0.3132	10.6747	4×10^{-4}	6×10^{-5}
Ag35nm	0.2997	10.7355	1011	45	0.2999	10.7384	7×10^{-4}	3×10^{-4}
Ag50nm	0.2522	10.8507	531	21	0.2512	10.8416	1×10^{-3}	7×10^{-4}
Ag65nm	0.2047	10.9659	339	13	0.2043	10.9639	$9{,}3 \times 10^{-4}$	2×10^{-4}

Table 2. *Table of extracted values for refractive indices from the fit program described in section 2.2. Starting from known values of refractive indices (columns n and k) taken from* Ciesielski *[23], subsequent FWHM and Δf characteristics are calculated and displayed. The extracted n_{fit} and k_{fit} are then displayed. The relative errors are shown in the last two columns. It tends to show that the errors coming from the numerical treatment of the data is negligible compared to some other sources of errors discussed in this section. Note that calculations were lead in python with numpy 128 bit floats instead of regular 64 bit floats, otherwise erroneous results are returned due to the (lack of sufficient) numerical precision. Note also that the table is indicative, as changing the span over which n and k are swept changes (slightly) the quality of the local linear fit, hence the relative error displayed here (see main text). Furthermore, when the thickness increases, the rounding errors also increase because of faster varying-surfaces (hence worsening the linear fit quality for a constant span, see Fig. 3)*

Another numerical error comes from the numerical extraction of FWHM and Δf from the transmission and reflection curves that are obtained experimentally. This numerical extraction induces errors on these values, hence subsequently influencing the extracted set of n and k. The error on Δf is estimated to be of the order $\pm 4\%$ and the error on FWHM to be on the order of 3×10^{-3}. In the case of a 50 nm layer with characteristic values as in Table 2, this leads to an estimated upper bound (i.e. error when the Δf and FWHM are both taken higher than their actual value) for this error of 4.3% for n and 1.1% for k. The lower bound, on the other hand, is estimated to be of 5.1% for n and 1.3% for k.

Optical alignment

The error made from each different optical alignment, i.e. each different realization of the alignment protocol, is estimated to be on the order of $\pm 5\%$ for Δf and $\pm 1\%$ for FWHM. We attribute this shift to the fact that the beam waist is of 71 µm, so that any small change of alignment will probe a slightly different region of the silver layer, hence giving a slighly different averaged index of refraction. Indeed, there is an approximate 70 µrad freedom on the input mirror setting to keep a good coupling, which corresponds to an approximate 5 µm change in beam position upon incidence on the quartz.

Changing the optical alignment procedure from one polarization axis (fast or slow, see setup description 2.4) to the other on the QR does not modify the results significantly.

Let us stress that one of the requirements that leads to the use of this particular technique is the experimental impossibility to vary the angle of incidence on the quartz by more than 2°, so

that any optical angular misalignment is contained within a fraction of this quantity. Once again, taking an example with the 50 nm thick silver layer, this leads to an upper bound error (defined as in the previous paragraph) of 4.5% for n and 1% for k. The lower bound, on the other hand, is calculated to be 5.3% for n and 1.1% for k. When calculated for 35 nm and 65 nm, the numbers stay in the same order of magnitude.

Deposition thickness

The deposition thickness uncertainty is estimated to be ±3 nm (corresponding to about 2 s of deposition time) for any given sample with respect to the nominal thickness value. This is estimated through depositing the thin films onto a silicon wafer, cleaving it and measuring the deposited film's thickness through Scanning Electron Microscopy (SEM).

This fixed uncertainty incidentally implies that it weights more on the smaller thicknesses. The results are displayed in Table 3.

		20 nm	35 nm	50 nm	65 nm
Upper Bound	n	9.2%	5.6%	4.3%	3.6%
	k	7.5%	4.6%	3.1%	2.2%
Lower Bound	n	7.9%	6.7%	4.4%	3.7%
	k	9.2%	5.4%	3.4%	2.4%

Table 3. *Table of errors due to thickness, with an uncertainty of* ±3 pm. *"Upper bound" means the set of solutions n_0 and k_0 are calculated for a certain set of FWHM and Δf with a thickness of $x + 3$ nm, whereas the lower bound is the opposite.*

Note that the thickness uncertainty, however, has a particular status within the accounted errors. Indeed, upon evaluation of a particular area's refractive index, the same systematic error is made at room or cryogenic temperature. For this reason, we evaluate the uncertainty with and without this error taken into account in Table 1.

Thickness at cryogenic temperature

Thermal expansion and contraction is a phenomenon which is mostly known and measured for bulk materials [27], and it does not change much with the heat treatment (annealing) or deposition conditions [28]. However, the thin-film Coefficients of Thermal Expansion (CTE) are shown to vary from their bulk counterpart (see [29] [30] [31]), so that the thickness is not only altered by the temperature, but it is altered in a different pattern than what we are able to calculate, due to the lack of available data on thermal expansion for silver thin films.

For the needs of calculating an approximative total contraction between room temperature and cryogenic temperature, we have used the integrated CTEs over the whole range of temperature for bulk material [32] [33] [34].

This leads to a raw total contraction coefficient (i.e. without taking the thin-layer nature of our sample) of:

$$\alpha^{\text{tot}}_{\text{300K-4K}} = -4{,}26 \times 10^{-3} \tag{11}$$

Fang [30], however, shows that the rough order of magnitude of change in CTE is of about a factor 1/2 for Ti and Al thin films.

Extrapolating this result to silver, this means that the actual coefficient for contraction $\alpha^{\text{tot}}_{\text{300K-4K}}$ could be comprised between the previously claimed value, $-4{,}26 \times 10^{-3}$, and half of this value.

Including the original uncertainty on the deposited thickness as well as the contraction uncertainty, the total uncertainty on the thickness at cryogenic temperature yields:

$$\Delta d^{4\mathrm{K}} = \Delta d^{300\mathrm{K}} + \Delta\alpha^{\mathrm{tot}} d^{300\mathrm{K}} + \alpha^{\mathrm{tot}} \Delta d^{300\mathrm{K}} \tag{12}$$

hence for a 50 nm thick layer

$$\Delta d^{4\mathrm{K}} \approx 3\,\mathrm{nm} + 7 \times 10^{-2}\,\mathrm{nm} \approx 3\,\mathrm{nm}$$

which can be essentially identified with the uncertainty of the deposited layer itself. This source of uncertainty is therefore discarded in the following, with the direct consequence that there is no difference in uncertainty between the room and cryogenic temperature.

3.2. Statistical analysis

In order to analyze the propagation of errors on the different parameters discussed throughout this session, we perform a *Monte-Carlo* type analysis. Because there is no obvious analytical dependence of the extracted n and k on the different variables fed to the program, in order to obtain an estimation of the total error made on the extracted set of values for n and k , the extraction program is run many times with slightly different values of FWHM, Δf and thickness d.

We evaluate the error on the FWHM and Δf to be distributed in a Gaussian fashion, that is, following a so-called normal distribution, by repeating many times the central value numerical extraction. The amplitude of the error is reported in the previous sections.

The error distribution on the thickness deposition is not directly measurable, because measuring a statistical error distribution on such deposition would require a large amount of runs and proper means of measuring the exact deposited thickness. By using the operator's experience about the deposition machine and the central limit theorem, however, we consider that all the possible errors in the process would lead to another normal (Gaussian) distribution.

Once those different sources of uncertainty are taken into account, the extraction program is run numerous times, by varying the input FWHM, Δf and thickness d following a normal distribution, each centered on their theoretical values and with a deviation dictated by the previously discussed values: A deviation of 2 nm is taken for the thickness deposition, of 4% for Δf and of 7×10^{-3} for FWHM. These values are selected so that the returned value from their respective normal distribution barely ever exceeds the nominal error value discussed in the previous sections, which are all the maximum recorded variations. An example of a distribution obtained by this mean is presented in Fig. 5. The calculations is lead for 35 nm, 50 nm and 65 nm. The results are presented and listed in Table 4.

These error, however, account for the uncertainty of the thickness, which is useful when treating the total uncertainty of the claimed values but lose their interest when treating the relative uncertainty between the room temperature and cryogenic values. The same systematic error on the thickness is made between room temperature and cryogenic temperature, as previously discussed, so that the uncertainties without taking into account the thickness are also calculated and presented in Table 5. These two Tables 4 and 5 are used to set the error bars in Table 1.

4. Conclusion

We have shown that it is possible to retrieve the refractive index of the metallic layers deposited on a quartz crystal resonator used as a *Fabry-Perot* cavity from the FWHM of the transmission peak and Δf, the frequency shift between the transmission and reflection peaks. We can achieve a satisfactory uncertainty on the measurement to differentiate the refractive indices between the room temperature and the 4 K measurement: for a 50 nm layer of silver for example, the refractive

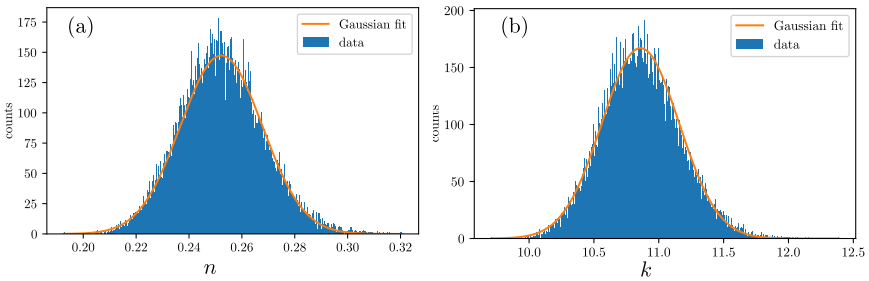

Fig. 5. Monte-Carlo *method to evaluate the error on n (a) and k (b) for a* 50 nm*-thick silver layer, taking into account the uncertainties, all of them following a normal distribution around their expected value: on thickness d (deviation* ±2 pm*), FWHM (deviation* $\pm 7 \times 10^{-3}$*) and* Δf *(deviation* ±4%*). The gaussian fit is rather good and gives a typical deviation of about* 6.1% *on n and* 2.7% *on k, with central values for n and k equal to their nominal values to within* 1×10^{-5} *for n and* 7×10^{-4} *for k (see Table 4). Graphs are made with 500 bins on 22650 points.*

		35nm	50nm	65nm
error on central value	n	$9{,}9 \times 10^{-3}$	8×10^{-5}	$5{,}4 \times 10^{-4}$
	k	$7{,}6 \times 10^{-3}$	7×10^{-4}	$6{,}9 \times 10^{-4}$
deviation	n	7.1%	6.1%	5.5%
	k	3.4%	2.7%	2.5%

Table 4. *Error on central value of n and k for different deposition thickness, following a* Monte-Carlo *type simulation where thickness uncertainty is taken into account. This permits to give the overall expected uncertainty on values and results for n and k extraction in the Results section. Note that this uncertainty is valid for both the room temperature and the cryogenic temperature.*

index is found to be $\tilde{n}_{\mathrm{Ag}} = 0.2609 - 96359i$ at room temperature and $\tilde{n}_{\mathrm{Ag}} = 0.1100 - 8.8149i$ at 4 K which is in reasonable agreement with the scarcely available data from the literature. Although the method we use is limited to a small set of materials with absorptive properties and small thickness, it brings a good knowledge about the refractive index of the equivalent layer deposited on both sides of the substrate. It is possible to extend the method to other wavelengths in order to derive the refractive indices over a wide spectral range.

Funding

MESRI France for the research scholarship, Région Franche-Comté and Labex FIRST-TF with their funding dedicated to this program (ANR-17-EURE-00002, ANR-10-LABX-48-01) MIMENTO platform for the deposition technology and Oscillator IMP platform (Equipex) for reference frequencies (ANR-11-EQPX-0033-OSC-IMP).

Acknowledgments

K.R. wishes to thank Remo Giust for the fruitful discussions, as well as Marion Delehaye, Clément Lacroûte, Jacques Millo, Damien Teyssieux, Moustafa Abdel-Hafiz, Christophe Fluhr and David Vernier for their help with the theoretical and experimental questions encountered.

		35nm	50nm	65nm
error on central value	n	$2{,}4 \times 10^{-3}$	$3{,}7 \times 10^{-3}$	2×10^{-3}
	k	$6{,}9 \times 10^{-4}$	$7{,}6 \times 10^{-4}$	$5{,}5 \times 10^{-5}$
deviation	n	5.8‰	5.3‰	4.9‰
	k	1.2‰	1.5‰	1.9‰

Table 5. *Same as Table 4, except that the uncertainty on thickness has not been taken into account here for the reasons explained in the main text.*

Disclosures

The authors declare no conflicts of interest.

Data Availability

Data underlying the results presented in this paper are not publicly available at this time but may be obtained from the authors upon reasonable request.

A. Appendix: Expression for δ_R

δ_R can be shown to yield:

$$\begin{aligned}\delta_R = \arccos\Bigg(\Bigg[\Big\{&B^4(-2D-2)^2E^2sin^4(\epsilon) - 4(A^2E^2 - 2ABDE\cos(\epsilon)\\ &- 2ABE\cos(\epsilon) + 2AE^2 + B^2D^2 + 2B^2D + B^2 - 2BDE\cos(\epsilon)\\ &- 2BE\cos(\epsilon) + E^2)(-A^2E^2 + 2ABDE\cos(\epsilon) + 2ABE\cos(\epsilon)\\ &- 2AE^2 - B^2D^2\cos^2(\epsilon) - 2B^2D\cos^2(\epsilon) + B^2E^2sin^2(\epsilon)\\ &- B^2\cos^2(\epsilon) + 2BDE\cos(\epsilon) + 2BE\cos(\epsilon) - E^2)\Big\}^{\frac{1}{2}}\\ &- B^2(-2D-2)Esin^2(\epsilon)\Bigg] \Bigg/\\ &\Big[2(A^2E^2 - 2ABDE\cos(\epsilon) - 2ABE\cos(\epsilon) + 2AE^2 + B^2D^2\\ &+ 2B^2D + B^2 - 2BDE\cos(\epsilon) - 2BE\cos(\epsilon) + E^2)\Big]\Bigg)\end{aligned} \tag{13}$$

where $A = |\zeta_{210}R_{220}|^2$, $B = 2|\zeta_{210}R_{210}|$, $D = |R_{210}|^4$ and $E = 2|R_{210}|^2$.

References

1. R. L. Olmon, B. Slovick, T. W. Johnson, D. Shelton, S.-H. Oh, G. D. Boreman, and M. B. Raschke, "Optical dielectric function of gold," Phys. Rev. B **86** (2012).
2. M.-M. Dujardin and M.-L. Theye, "Investigation of the optical properties of Ag by means of thin semi-transparent films," J. Phys. Chem. Solids **32**, 2033–2044 (1971).
3. V. B. Svetovoy, P. J. van Zwol, G. Palasantzas, and J. T. M. De Hosson, "Optical properties of gold films and the Casimir force," Phys. Rev. B **77**, 035439 (2008).
4. M. Mayy, G. Zhu, E. Mayy, A. Webb, and M. A. Noginov, "Low temperature studies of surface plasmon polaritons in silver films," J. Appl. Phys. **111**, 094103 (2012).
5. H. Reddy, U. Guler, A. V. Kildishev, A. Boltasseva, and V. M. Shalaev, "Temperature-dependent optical properties of gold thin films," Opt. Mater. Express **6**, 2776 (2016).
6. S. A. Maier and H. A. Atwater, "Plasmonics: Localization and guiding of electromagnetic energy in metal/dielectric structures," J. Appl. Phys. **98**, 011101 (2005).

7. S. Galliou, M. Goryachev, R. Bourquin, P. Abbé, J. P. Aubry, and M. E. Tobar, "Extremely Low Loss Phonon-Trapping Cryogenic Acoustic Cavities for Future Physical Experiments," Sci. Reports **3** (2013).
8. J. Bon, L. Neuhaus, S. Deléglise, T. Briant, P. Abbé, P.-F. Cohadon, and S. Galliou, "Cryogenic optomechanic cavity in low mechanical loss material," J. Appl. Phys. **124**, 073104 (2018).
9. IEEE, "ANSI/IEEE Std 176-1987 An American National Standard IEEE Standard on Piezoelectricity," p. 74 (1987).
10. J. Bon, R. Bourquin, J.-J. Boy, and S. Galliou, "Frequency–Temperature Compensated Cuts of Crystalline-Quartz Acoustic Cavity Within the Cryogenic Range [4 K, 15 K]," IEEE Transactions on Ultrason. Ferroelectr. Freq. Control. **65**, 1738–1740 (2018).
11. G. S. Agarwal and S. S. Jha, "Multimode phonon cooling via three-wave parametric interactions with optical fields," Phys. Rev. A **88** (2013).
12. M. Aspelmeyer, T. J. Kippenberg, and F. Marquardt, "Cavity Optomechanics," Rev. Mod. Phys. **86**, 1391–1452 (2014).
13. K. A. Nelson, "Stimulated Brillouin scattering and optical excitation of coherent shear waves," J. Appl. Phys. **53**, 6060–6063 (1982).
14. P. Kharel, G. I. Harris, E. A. Kittlaus, W. H. Renninger, N. T. Otterstrom, J. G. E. Harris, and P. T. Rakich, "High-frequency cavity optomechanics using bulk acoustic phonons," Sci. Adv. **5**, eaav0582 (2019).
15. K. Rosenziveig, J. Bon, P. Abbe, V. Soumann, R. Giust, N. Passilly, P.-F. Cohadon, and S. Galliou, "Quartz Crystal Resonator Used as an Optical Fabry-Perot Cavity for Optomechanical Coupling," in *2020 Joint Conference of the IEEE International Frequency Control Symposium and International Symposium on Applications of Ferroelectrics (IFCS-ISAF),* (IEEE, Keystone, CO, USA, 2020), pp. 1–5.
16. M. Bass and J. Bennett, "Optical Properties of Metals," Tech. rep., University of Southern California Los Angeles center for LASER studies (1983).
17. D. Smith and F. Fickett, "Low-Temperature Properties of Silver," J. Res. Natl. Inst. Standards Technol. **100**, 119 (1995).
18. H. Reddy, U. Guler, K. Chaudhuri, A. Dutta, A. V. Kildishev, V. M. Shalaev, and A. Boltasseva, "Temperature-Dependent Optical Properties of Single Crystalline and Polycrystalline Silver Thin Films," ACS Photonics **4**, 1083–1091 (2017).
19. M. P. Nezhad, A. Simic, and Y. Fainman, "Measurement Of The Optical Properties Of Gold At Cryogenic Temperatures," in *Frontiers in Optics 2010/Laser Science XXVI,* (OSA, Rochester, New York, 2010), p. FThR4.
20. J. J. Monzón and L. L. Sánchez-Soto, "On the concept of absorption for a Fabry–Perot interferometer," Am. J. Phys. **64**, 156–163 (1996).
21. J. J. Monzón and L. L. Sánchez-Soto, "On the definition of absorption for a Fabry-Perot interferometer," Pure Appl. Opt. J. Eur. Opt. Soc. Part A **1**, 219–226 (1992).
22. R. Giust, J.-M. Vigoureux, and M. Sarrazin, "Asymmetrical properties of the optical reflection response of the Fabry–Pérot interferometer," J. Opt. Soc. Am. A **17**, 142 (2000).
23. A. Ciesielski, L. Skowronski, M. Trzcinski, and T. Szoplik, "Controlling the optical parameters of self-assembled silver films with wetting layers and annealing," Appl. Surf. Sci. **421**, 349–356 (2017).
24. J. W. Weber, V. E. Calado, and M. C. M. van de Sanden, "Optical constants of graphene measured by spectroscopic ellipsometry," Appl. Phys. Lett. **97**, 091904 (2010).
25. H. U. Yang, J. D'Archangel, M. L. Sundheimer, E. Tucker, G. D. Boreman, and M. B. Raschke, "Optical dielectric function of silver," Phys. Rev. B **91**, 235137 (2015).
26. S. V. Jayanti, J. H. Park, A. Dejneka, D. Chvostova, K. M. McPeak, X. Chen, S.-H. Oh, and D. J. Norris, "Low-temperature enhancement of plasmonic performance in silver films," Opt. Mater. Express **5**, 1147 (2015).
27. K. O. McLean, "Low temperature thermal expansion of copper, silver, gold and aluminum," Ph.D. thesis, Iowa State University, Ames, Iowa (1969).
28. E. D. Marquardt, J. P. Le, and R. Radebaugh, "Cryogenic Material Properties Database," in *Cryocoolers 11,* (Keystone, CO, USA, 2000).
29. T.-C. Chen, W.-J. Lin, and D.-L. Chen, "Effect of temperature gradient on simultaneously experimental determination of thermal expansion coefficients and elastic modulus of thin film materials," J. Appl. Phys. **96**, 8 (2004).
30. W. Fang and C.-Y. Lo, "On the thermal expansion coefficients of thin films," Sensors Actuators A: Phys. **84**, 310–314 (2000).
31. A. E. Mag-isa, B. Jang, J.-H. Kim, H.-J. Lee, and C.-S. Oh, "Coefficient of thermal expansion measurements for freestanding nanocrystalline ultra-thin gold films," Int. J. Precis. Eng. Manuf. **15**, 105–110 (2014).
32. G. K. White and J. G. Collins, "Thermal expansion of copper, silver, and gold at low temperatures," J. Low Temp. Phys. **7**, 43–75 (1972).
33. D. B. Fraser and A. C. H. Hallett, "The Coefficient of Thermal Expansion of Various Cubic Metals Below 100 °K," Can. J. Phys. **43**, 193–219 (1965).
34. N. Waterhouse and B. Yates, "The interferometric measurement of the thermal expansion of silver and palladium at low temperatures," Cryogenics **8**, 267–271 (1968).